Journal of Magnetic Resonance Open 16-17 (2023) 100138

Contents lists available at ScienceDirect

Journal of Magnetic Resonance Open

journal homepage: www.sciencedirect.com/journal/journal-of-magnetic-resonance-open

MR based magnetic susceptibility measurements of 3D printing materials at 3 Tesla

Maitreyi Sangal [a,*], Maria Anikeeva [b,c], Simon C. Priese [a], Hendrik Mattern [a,d,e], Jan-Bernd Hövener [b,c], Oliver Speck [a,d,e,f]

[a] Department of Biomedical Magnetic Resonance, Otto-von-Guericke-University, Universitätsplatz 2, Magdeburg 39106, Germany
[b] Section Biomedical Imaging, Molecular Imaging North Competence Center (MOIN CC), Department of Radiology and Neuroradiology, University Hospital Schleswig-Holstein (UKSH), Kiel University, Am Botanischen Garten 14, Kiel 24118, Germany
[c] Department of Radiology and Neuroradiology, University Hospital Schleswig-Holstein (UKSH), Arnold-Heller-Straße 9, Kiel 24105, Germany
[d] Center for Behavioral Brain Sciences, Magdeburg, Germany
[e] German Center for Neurodegenerative Diseases, Magdeburg, Germany
[f] Leibniz Institute for Neurobiology, Magdeburg, Germany

ARTICLE INFO

Keywords:
Magnetic susceptibility
3D printing materials
MR compatible materials
Magnetic property database
MR quantitative susceptibility mapping

ABSTRACT

Commercial availability, ease of printing and cost effectiveness have rendered 3D printing an essential part of magnetic resonance (MR) experimental design. However, the magnetic properties of several materials contemporarily used for 3D printing are lacking in literature to some extent. A database of the magnetic susceptibilities of several commonly used 3D printing materials is provided, which may aid MR experiment design. Here, we exploit the capability of magnetic resonance imaging (MRI) to map the local magnetic field variations caused by these materials when placed in the scanner's $\mathbf{B_0}$ field. Exact analytical solutions of the magnetic flux density distribution for a cylindrical geometry are utilized to fit experimentally obtained data with theory in order to quantify the magnetic susceptibilities. A detailed explanation of the data processing and fitting procedure is presented and validated by measuring the susceptibility of air along with high resolution MR measurements. Furthermore, an initiative is taken to address the need for a comprehensive database comprising of not only the magnetic susceptibilities of 3D printing materials, but also information on the 3D printing parameters, the printers used, and other information available for the materials that may also influence the measured magnetic properties. An open platform with the magnetic susceptibilities of materials reported in this work besides existing literature values is provided here, with the aim to invite researchers to enable further extension and development towards an open database to characterize commonly used 3D printing materials based on their magnetic properties.

1. Introduction

The rapid development of 3D printing or additive manufacturing technology such as fused deposition modeling (FDM), stereolithography (SLA), selective laser sintering (SLS) or digital light processing (DLP), especially in the last decade, has made various 3D printers and 3D printing materials commercially available and economically feasible for wide ranging applications in the industrial and medical sector in educational and research institutions worldwide [1–5]. In particular, magnetic resonance imaging (MRI) experiments benefit considerably due to the possibility of 3D printing MR compatible and experiment specific objects efficiently and cost effectively [6]. This includes designing MR compatible phantoms [7], radiofrequency (RF) coil manufacturing [8], patient specific MR compatible and biocompatible surgical implants, prosthetics [9–12], prototypes for flow imaging in biological systems e.g. vasculature, aneurysm models [9–11], as well as technical systems such as packed bed reactors [12–14]. Thus, 3D printing has proved to be and continues to be an integral part of MR related applications.

The vast range of materials available for 3D printing, however, requires knowledge of their physical properties to be able to select materials matching a desired experiment. While many manufacturers do provide an overview of the thermal and mechanical properties, such as hardness, softness, tensile strength, flexibility, elasticity; the magnetic

* Corresponding author.
E-mail address: maitreyi.sangal@ovgu.de (M. Sangal).

https://doi.org/10.1016/j.jmro.2023.100138

Available online 14 November 2023

properties of several commonly used materials are typically missing. Especially in the context of MR related studies, knowledge of the magnetic susceptibilities of materials besides their MR properties is imperative.

The MR relaxation times (i.e. T_1, T_2) of a material impact its visibility or contrast in an MR experiment or setup. Commonly, housings of a coil, or structural support of an experimental setup is desired to be "MR invisible". However, even materials that do not deliver MR signal can impact the measurement results since the magnetic susceptibility impacts the magnetic field distribution around the object. Such magnetic properties can lead to local inhomogeneities of the magnetic field and, therefore, reduce the apparent transversal relaxation time T_2^*, leading to local signal dropouts. In addition, the resonance frequency shifts caused by the material's susceptibility can lead to geometric distortions of the reconstructed MR images. The extent of such geometric distortions is proportional to the difference in susceptibilities $\Delta\chi$ of two adjacent materials, the field strength B_0, and inversely proportional to the imaging bandwidth [15]. While these effects may be suppressed for a given field strength by varying the imaging sequence parameters like reducing the echo time T_E, increasing the bandwidth or changing the orientation of the objects with respect to the B_0 field, knowledge of the magnetic properties is relevant to avoid such unintended effects during the design of an experimental setup. In addition, it also enables one to calculate the field inhomogeneities caused by the objects in order to compensate for them.

Here is where the MR scanner itself comes into the picture by enabling quantification of the magnetic susceptibilities of the materials used. The MR signal-phase encodes the phase shift caused by resonance frequency variations due to local field inhomogeneities that arise from the magnetic susceptibility of the object placed in the MR scanner's static B_0 field [16]. There are different approaches to perform MR based measurements of magnetic susceptibilities [15,17–19]. One well known approach to measure the magnetic susceptibility of a material that itself may not give an MR signal, is to map the field changes caused by it with respect to an MR visible reference medium of known susceptibility.

So far, the largest database of the magnetic susceptibility of different materials typically used for MR experiments, e.g. glasses, polymers, silicones, polyurethanes, 3D printing filaments and glues, was published in [19] which provided comparison with earlier works [17,20]. Following this, another MR based susceptibility measurement method with the values for some commonly used 3D printing materials was provided in [21]. Nevertheless, most of the materials provided in these works do not have accepted 'reference' literature values yet. Replication and extension of scarce literature values and collection of known properties in a reference database of susceptibility measurements of several contemporarily available 3D printing materials is the main goal of this contribution.

In this work, we utilize a 3T MR scanner (Skyra, Siemens Healthineers, Erlangen) to quantify susceptibility using the approach mentioned above [19]. We provide a detailed explanation of the several preprocessing steps needed to be performed on the MR acquired phase images to quantify the susceptibility in Methods (Section 2). This is followed by a description of the procedure used for fitting the data with theory, and finally also a validation measurement of the susceptibility of air which is well known at normal temperature and pressure (NTP) [22]. This will allow researchers to replicate and further extend our database. In order to test if the chosen voxel resolution is sufficient to accurately extract the geometry of the 3D printed object, we also present the reproducibility of our results with a higher resolution experiment for selected materials, and finally conclude with comparison of the results for some of the materials, which are common with the previous literature. All the results are finally also provided on the following open platform: **MaDaMEPro** (**Ma**terial **Da**tabase for **M**agn**E**tic **Pro**perties, https://madamepro.ovgu.de) which is an initiative to build a comprehensive database with magnetic properties of commonly used 3D printing materials, and is open to further contribution and development from the scientific community.

2. Methods

2.1. 3D printers and materials

For this work, we used three fused deposition modeling (FDM) printers (S5, Ultimaker, i3 MK3S+, Prusa, and Stratasys Fortus 380 mc) for printing with filaments; and one stereolithography (SLA) printer (Formlabs, Form 3) to print with liquid resins. A total of 22 different materials were used including 15 different filaments and 7 liquid resins (see Table 1).

For magnetic susceptibility measurements, a single "large" cylinder was printed with each material, with 100 mm length (L) and 10 mm diameter (D) such that the aspect ratio (L/D) was 10:1 (denoted as 10 throughout the rest of this work). All the 3D printed cylinders are shown in Fig. 1(a) with filaments on the left with yellow name labels and resins on the right with blue name labels. Note that only for one filament material (ABS), two different print settings were chosen as explained below, resulting in an extra 3D printed cylinder. Each cylinder was tightly secured in the screw cap of a plastic (PP) bottle, and then immersed in the bottle filled with deionized water (Fig. 1(b)). This ensured the cylinder's long axis to almost coincide with the axis of the bottle and hence be fixed in the center. Throughout the rest of the work, all references to the 'axis of the cylinder', unless otherwise specified, imply the cylinder's 'long axis'.

Print parameters for FDM prints: Each cylinder was printed with 100 % infill density and triangular infill pattern and 0.3 mm layer

Table 1
Materials used for our experiments; Filaments on top and resins below. Note that (1) for ABS two types of infill densities, 50 % and 100 %, were tested. (2) Cylinders from PLA were printed in two colors: red and green.(3) The numbers like 85A, 95A and 98A for the TPU materials as well as for resins, denote the shore hardness of the materials, 98A being the hardest. These values are listed only where they were provided by the manufacturer and to distinguish the three TPU cylinders based on their Shore A hardness. Further details about the chemical compositions of the resins may be found in [23–29].

Filaments		
Material	Manufacturer	FDM Printer
Acrylonitrile butadiene styrene (ABS) (1)	Ultimaker	Ultimaker
Polylactic acid (PLA) (2)	Ultimaker	Ultimaker
Polylactic acid *tough* (PLA tough)	Ultimaker	Ultimaker
Co-polyester (CPE)	Ultimaker	Ultimaker
Co-polyester *resistant* (CPE+)	Ultimaker	Ultimaker
Polyethylene terephthalate glycol (PETG)	Ultimaker	Prusa i3mk3S+
Polycarbonate (PC)	Stratasys	Stratasys Fortus 380 mc
Polyamide (Nylon)	Ultimaker	Ultimaker
Polypropylene (PP)	Ultimaker	Ultimaker
Thermoplastic Elastomer (TPE)	Tefabloc, Verbatim	Prusa i3mk3S+
Thermoplastic polyuerthane, Shore hardness 85A (TPU 85A) (3)	NinjaTek	Prusa i3mk3S+
Thermoplastic polyuerthane, Shore hardness 95A (TPU 95A)	Polyflex, Polymaker	Prusa i3mk3S+
Thermoplastic polyuerthane, Shore hardness 98A (TPU 98A)	Flexfill, Filamentum	Prusa i3mk3S+
Recycled polyethylene terephthalate (rPET)	BASF, Ultrafuse	Prusa i3mk3S+
Resins		
Material	Manufacturer	SLA Printer
Clear V4	Formlabs	Formlabs Form 3
Dental LT V2	Formlabs	Formlabs Form 3
Durable V1	Formlabs	Formlabs Form 3
Elastic 50A	Formlabs	Formlabs Form 3
Flexible 80A	Formlabs	Formlabs Form 3
Rigid 10K	Formlabs	Formlabs Form 3
Tough 1500 V1	Formlabs	Formlabs Form 3

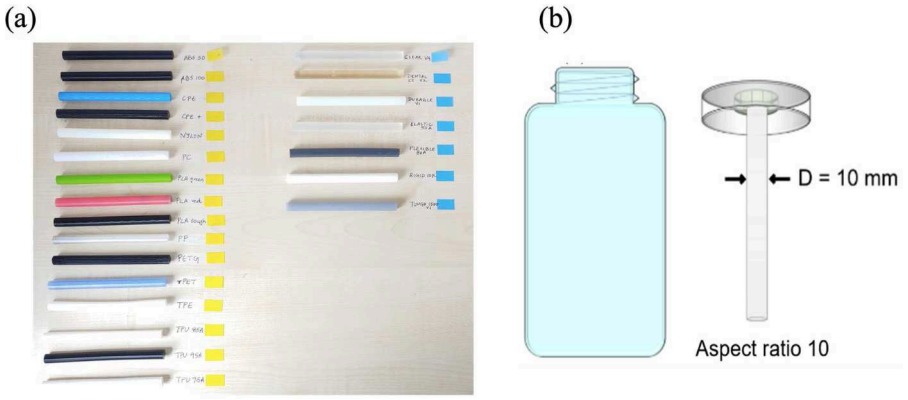

Fig. 1. (a) Picture of the 3D printed cylinders for all the materials used in this work. On the left are all the cylinders printed with filamens. On the right are the ones printed with resins. Note that the materials are arranged in the same order as they appear in Table 1 and Table 3.(b): Experimental setup. A large cylinder (100 mm length, 10 mm diameter) immersed in deionized water. The diameter of the bottle itself was 60 mm.

height. Only for ABS, the cylinders were printed with 50 % as well as 100 % infill density to check how varying the print settings may affect the measurement results.

Print parameters for SLA prints: A print resolution of 0.1 mm was used for the Clear V4, Durable V1, Tough 1500 V1, Dental LT V2 and Elastic 50A resins; and 0.05 mm for Flexible 80A and Rigid 10 K resins.

2.2. Susceptibility measurements

2.2.1. Theoretical background & experimental setup

***Background theory and phantom preparation*:** When objects are placed in the MR scanner which has a magnetic flux density $\mathbf{B_0}$, they experience a magnetization $\mathbf{M}$ and thereby perturb the field locally depending on their magnetic susceptibility, χ. For linear materials i.e. materials with no preferred magnetization direction, this induced magnetization is directly proportional to the applied external magnetic field $\mathbf{H}$ as $\boldsymbol{M} = \chi\mathbf{H}$ and hence the magnetic flux density distribution $\mathbf{B}$, around them (in SI units) is [15,16,30]

$$\mathbf{B} = \mu_0(\mathbf{H}+\mathbf{M}) = \mu_0(1+\chi)\frac{\mathbf{M}}{\chi} \tag{1}$$

where μ_0 is the magnetic permeability of vacuum and χ is the volume magnetic susceptibility which is dimensionless in SI units. In this work, χ denotes volume magnetic susceptibility.

This perturbation to the external magnetic field $\mathbf{\Delta B}$ (where $\mathbf{\Delta B = B - B_0}$), which is caused due to the magnetic susceptibility of the object manifests as a shift in the local Larmor precession frequency $\Delta\omega = \gamma\Delta B$, and hence a shift in the phase $\Delta\phi = \gamma\Delta B T_E$ of the freely precessing nuclear spins. Here γ is the gyromagnetic ratio of the nuclei and T_E is the echo time or time of acquisition.

Thus, mapping the spatial distribution of the phase shift $\Delta\phi$ allows one to map the variation in magnetic flux density arising due to the object's susceptibility, using appropriate pulse sequences and post processing techniques. For materials with simple geometries such as a sphere or a cylinder, analytical expressions of the flux density distribution are well known [15,16,30] and can be exploited to compare theory with experimental measurements to quantify the magnetic susceptibility χ.

Since 3D printing smooth spheres can be problematic due to increased surface imperfections and in many cases a degraded print quality, we chose to print long cylinders with an aspect ratio of 10 (Fig. 1 (b)) such that the theoretical expression for the flux density distribution around an infinitely long cylinder can be fitted with the experimentally obtained field maps. While, this approximation is sufficient for a large enough aspect ratio, it may lead to errors in susceptibility quantification since most materials investigated here may be weakly magnetic (Fig. 2 (b)). Hence, we utilize the exact analytical expression for the flux density distribution around a finite sized cylinder derived in [31] for our estimation, which was implemented in a MATLAB code.

The magnetic flux density distribution depends on the size and orientation of the cylinder's axis with respect to the direction of the external field. Since the materials investigated here themselves may not give an MR signal, the cylinder for each material was immersed in deionized water serving as a reference medium of known susceptibility $\chi_{H2O} = -9.04$ ppm [15,22] (Fig. 1(b)), and the field change was mapped in the water surrounding the cylinder. For mapping the field outside the cylinder, the most suitable orientation of the cylinder is where its axis is orthogonal to the $\mathbf{B_0}$ field.

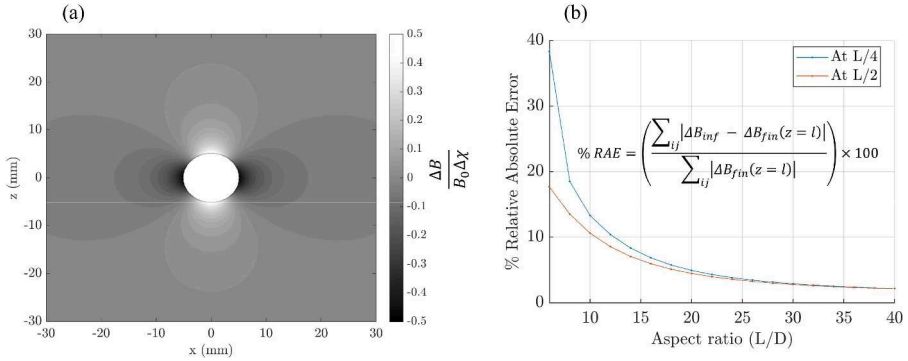

Fig. 2. (a) The magnetic flux density distribution outside a finite sized cylinder of aspect ratio 10 with magnetization orthogonal to its long axis (along z direction here). (b) Percentage relative absolute error (%RAE) between the infinite approximation ΔB_{inf} and the exact expression ΔB_{fin} (Eq. (2)) vs. different aspect ratios (L/D) for a transverse cross section at the center of the cylinder y = L/2 (orange) and at y = L/4 (blue).

The expression for the component of **ΔB** along the direction of the external field outside a cylinder with its axis oriented orthogonal to the $\mathbf{B_0}$ field is shown in Eq. (2). Here, the z component ($\mathbf{\Delta}B_z$) is given since the scanner's field is conventionally along the z direction. Fig. 2(a) is the simulated $\mathbf{\Delta}B_z$ outside a finite sized cylinder with an aspect ratio of 10, and its axis orthogonal to $\mathbf{B_0}$. Additionally, Fig. 2(b) depicts the percentage relative absolute error (%RAE) between the magnetic flux density distribution for the same orientation of the cylinder's axis with respect to the $\mathbf{B_0}$ field, using the infinitely long cylinder approximation and the exact solution vs different aspect ratios (L/D). Note that at an aspect ratio of 10, the infinite approximation differs from the exact expression by more than 10 % even at the cross-sectional plane passing through the center of the cylinder (i.e. at L/2), indicating the importance of using the exact analytical solution for the purpose of fitting.

$$\Delta B_z = \frac{\Delta\chi B_0}{2\pi}\left(\frac{R}{\rho}\right)\left[\cos^2\phi(A_1 + 2A_2) - 2A_2\right] \tag{2}$$

where $A_1 = \beta_+ P_4(k_+) - \beta_- P_4(k_-)$, $A_2 = \beta_+ P_3(k_+) - \beta_- P_3(k_-)$.

The functions P_3 and P_4 are auxiliary functions defined in [31] (Eqns. 20,22) involving elliptical integrals of the first, second and third kind and

$$\beta_\pm = \frac{y \pm L_h}{\sqrt{(y \pm L_h)^2 + (\rho + R)^2}};$$

$$k_\pm = \sqrt{\frac{(y \pm L_h)^2 + (\rho - R)^2}{(y \pm L_h)^2 + (\rho + R)^2}}$$

Here L_h is half the total length (L) of the cylinder, R is the radius of the cylinder, y is the y coordinate along the axis of the cylinder and $\rho = \sqrt{(x^2 + z^2)}$,$\phi$ is the azimuthal angle and $\Delta\chi = \chi - \chi_{H2O}$. The above equation is valid for weakly magnetic materials (i.e. for $|\chi| << 1$).

***Sequence and imaging parameters*:** Typically, GRE sequences are used for mapping susceptibility differences since they are sensitive to detect signal phase changes that are caused by local field inhomogeneities. Thus, a 3D dual echo gradient recalled echo (FLASH) sequence was used to acquire phase maps at 3T (Skyra, Siemens Healthineers, Erlangen) using a 32 channel head RF coil. Sequence parameters were: flip angle 15°, $T_{E1} = 2$ ms, $T_{E2} = 7$ ms, TR = 30 ms, FOV 80 × 160 × 80 mm, 1.0 mm isotropic voxel resolution.

***Data acquisition*:** For each RF channel 'c' and for each echo, the signal magnitude and phase images were acquired separately. The channel combined magnitude images were also acquired.

2.2.2. *Post processing*:

Following data acquisition, to obtain the $\Delta\phi$ phase maps, several post processing steps were performed in order to isolate the local phase shifts arising solely due to the magnetic susceptibility of the materials. For this purpose, tools from the QSMbox software [32,33] were used. The post processing steps performed in this work are broadly divided in two parts:

(1) Post processing 1: This part consists of the steps required to obtain the channel-combined phase maps $\Delta\phi$, starting from the channel-combined magnitude images, using tools in QSMbox.
(2) Post processing 2: Once, the $\Delta\phi$ maps are obtained, further steps are needed to be done before fitting the data with Eq. (2), such as background field removal and choosing the ROI for fitting.

Fig. 3 is a flowchart giving an introduction to the post-processing steps that are performed in this work. These post processing steps are further explained in this section by taking Clear resin V4 as an example material. In Figs. 4, 5 and 6, the phase maps are shown for slice number 80 for Clear resin V4:

***Post processing 1. Masking*:** From the channel combined magnitude images, a mask was created such that the water filled region that provides MR signal is the region of interest (ROI), and the region occupied by the cylinder inside the bottle, as well as all regions of air surrounding the bottle in the FOV were considered as 'background' and excluded from the ROI.

***Phase offset removal and echo combination per RF channel*:** An initial phase offset ϕ_0 is present for each RF channel 'c', and is different for each channel depending on its sensitivity, position relative to the FOV and echo time. Several approaches exist for finding these phase offsets [34,35]. However, we utilized the POEM method [36] which is

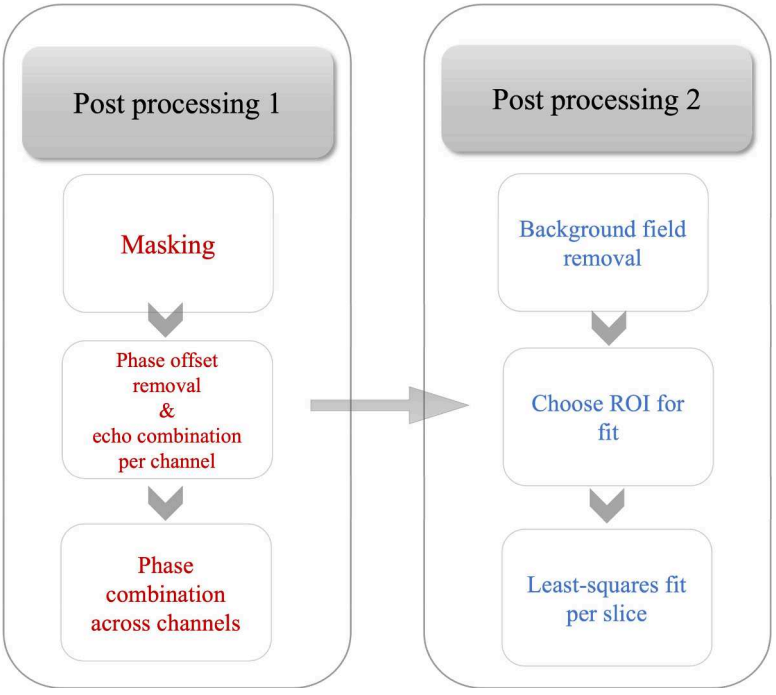

Fig. 3. Flowchart summarizing the post-processing procedure used in this work.

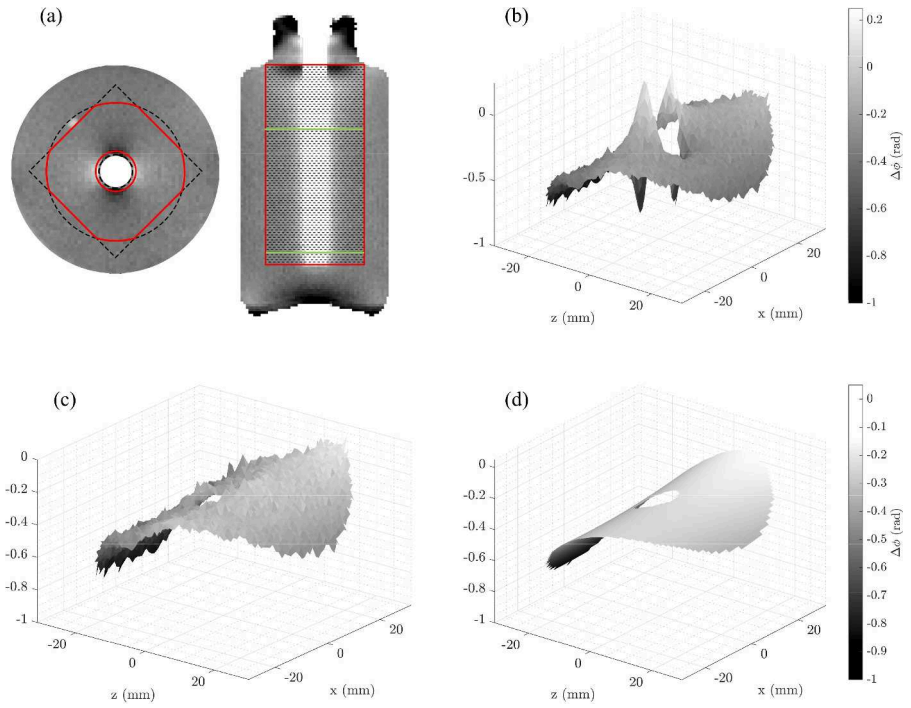

Fig. 4. (a) Region showing pixels chosen for the fit. The region bounded between the solid red curves in a 'squircle' is used for fitting. (b) The combined phase map $\Delta\phi$. (c) The residual background phase. (d) The simulated quadratic background phase using Eq. (4). Note the gray scale for (c) and (d) is the same.

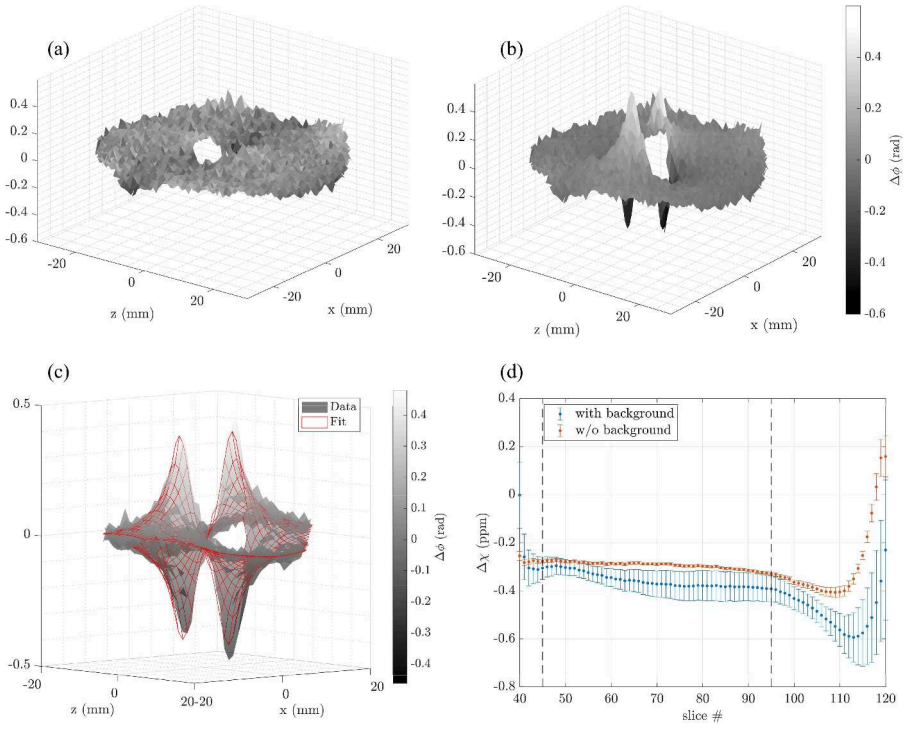

Fig. 5. (a) Residual map between the extracted and simulated $\Delta\phi_{\text{background}}$ (Fig. 4(c), (d) respectively). (b)The background phase filtered $\Delta\phi$ map. Note that the gray scale is the same for (a) and (b). (c) Example of the fit for one slice. (d) The fitted $\Delta\chi$ with (blue) and without (orange) the background phase vs slices where the cylinder is clearly visible.

implemented in QSMbox, does not require having a reference scan, or a measure of the coil sensitivities and is relatively computationally inexpensive. This method is also equivalent to the MCPC-3D-S approach [37]. After removing these phase offsets, the corrected phase is obtained which needs to be spatially unwrapped because the phase can only be registered in a 2π range. This was done using the implementation of the 3D best path phase unwrapping method [38] in QSMbox. Subsequently, a temporal phase unwrapping is performed across both echo times and then the phase is echo combined assuming it grows linearly with time, using a magnitude weighted linear least squares fit (based on [36]).

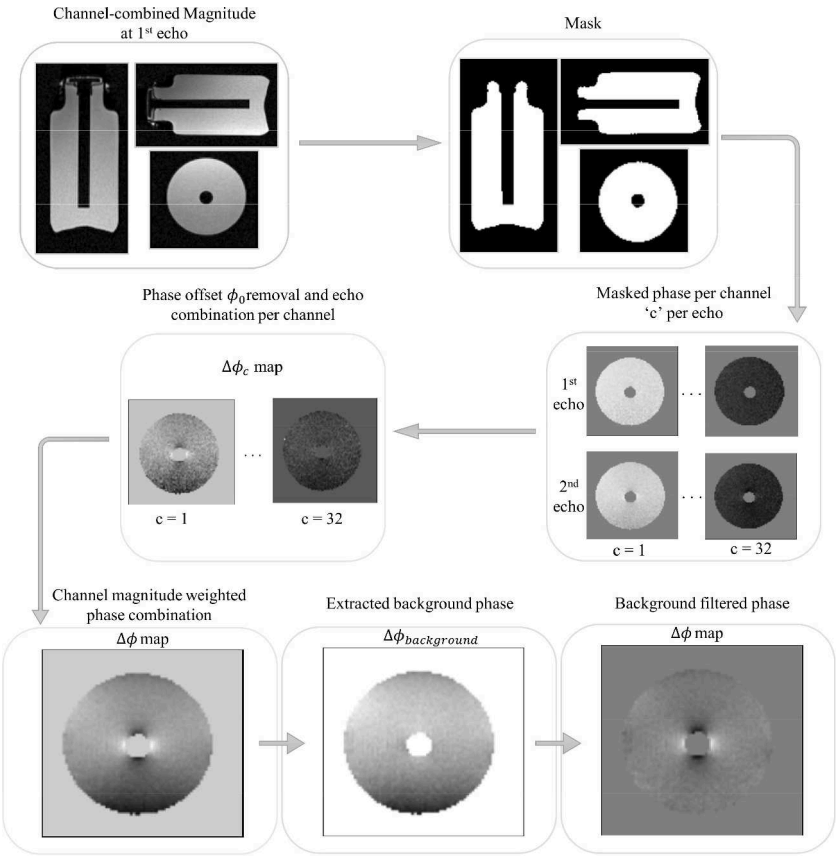

Fig. 6. Flowchart summarizing all the post processing steps required to obtain the background phase filtered $\Delta\phi$ map only due to the susceptibility of the cylinder material. All orthogonal views are only shown for the magnitude and mask images. Only the short axis view (i.e.x-z plane, with the B_0 field along z) for a slice along the cylinder's axis is shown for the phase maps.

Finally, a phase corrected, unwrapped and echo combined phase map $\Delta\phi_c$ is obtained for each RF channel.

Phase combination across channels: Following this, the phase across all channels was combined using a magnitude weighted complex summation of the complex signals for each channel

$$S_{combined} = \frac{\sum_{c=1}^{N} M_c e^{i\phi_c}}{\sum_{c=1}^{N} M_c} \tag{3}$$

where M_c is the echo combined signal magnitude which is combined using sum of squares (SoS) [34], ϕ_c is the corrected phase map for each channel 'c'. The combined phase map, $\Delta\phi = \angle(S_{combined})$ is then unwrapped again as above because the complex summation results in the phase being wrapped in the 2π range.

Post processing 2. Background field removal: It is important to note that the resultant phase map $\Delta\phi$ still comprises of phase shifts due to the background field $\Delta\phi_{background}$ (Fig. 4(b)), which is present due to imperfect magnetic field homogeneity, eddy currents and other sources of susceptibility outside the ROI as well as inside the ROI (such as presence of air bubbles). Hence, one needs to ideally have a measure of the background field. One approach is to have a reference scan without the material in consideration and only with water which can be then subtracted from the phase maps measured with the material inserted. However, any changes in position of the phantom while removing and inserting new materials would result in a change in this background field, thus requiring a separate reference scan for each material. Besides this several background field removal approaches exist which apply spatial filtering methods to remove the phase shift arising due to susceptibility sources outside the ROI [39,40].

In our case where the cylinder itself is excluded from the ROI, using these methods will filter out the phase shifts induced by the material of interest (cylinder). Thus, the optimal approach for us was to simulate this background phase $\Delta\phi_{background}$ for each material (similar to [9]). This was done iteratively by first performing a least squares fit on the obtained phase map $\Delta\phi$ using Eq. (2) to obtain an initial estimate of $\Delta\chi$. Using this value, a new phase map was estimated which was then subtracted from the original $\Delta\phi$. The residual resulted in the background phase (Fig. 4(c)), which was then fitted with a quadratic function to obtain:

$$\Delta\phi_{Background} = a + b_x x + b_z z + c_{xx}x^2 + c_{xz}xz + c_{zz}z^2 \tag{4}$$

This simulated background phase (Fig. 4(d)) was subtracted from the original $\Delta\phi$ to get a background phase filtered map (Fig. 5(b); Fig. 5(a) is the residual between the extracted and simulated background phase (Fig. 4(c),(d)). This filtered phase map was fitted per slice with Eq. (2) to obtain a final estimate of $\Delta\chi$. Fig. 5(c) is an example the fit for slice #80 with the $\Delta\phi$ map in greyscale and the fitted Eq. (2) plotted over as the red transparent mesh. Fig. 5(d) depicts the fitted $\Delta\chi$ values versus slice numbers for Clear resin V4 both with (orange) and without (blue) removing the background field. Carefully removing the background field results in a better fit with reduced error as well as lower variation of the estimated $\Delta\chi$ over slices. Here slice #40 corresponds to the bottom most part of the cylinder. Slice #120 pertains to 8 cm upwards along the cylinder in the region near the bottle cap. The two black dashed lines enclose the slices corresponding to 5 cm along the length of the cylinder which are chosen for averaging (explained below). Fig. 6 depicts all the post processing steps to obtain a background field filtered $\Delta\phi$ map in a diagrammatic representation.

Choosing data for fit: Having obtained the background phase filtered $\Delta\phi$ maps we chose certain number of slices as well as a region of

pixels per slice to be included in the fitting process. First, the slices along the length of the cylinder, where the cylinder is clearly visible below the neck of the bottle were chosen. This is highlighted by the red rectangle in Fig. 4(a) on the right. For each slice, the pixels to be included for fitting were chosen as marked by the region included between the red lines in Fig. 4(a) on the left, corresponding to an intersection of a square and a circle in black dotted lines [41]. Moreover, the regions inside the cylinder which do not give any signal were excluded (bounded by the small black dotted circle). Since the pixels very close to the cylinder-surface and water interface suffer from partial volume effects, these can be quite sensitive to the fitting process and so one extra layer of these pixels was also excluded (layer bounded by the black dotted circle corresponding to the 5 mm radius of the printed cylinder and the small red circle with a radius of 6 mm).

Least squares fit per slice: A least squares fit was then performed per slice for the defined region mentioned above, by fitting the experimentally obtained field maps with the simulated maps from Eq. (2). The fitted $\Delta\chi$ values per slice are shown in Fig. 5(d). However, since some slices close to the bottle cap and bottle-neck had more air bubbles present, as well as signal loss due to other susceptibility sources like the bottle cap itself, some slices near both ends of the cylinder were discarded before obtaining a slice-averaged estimate of $\Delta\chi$. Thus, for every material, a total of 50 slices was used for slice-averaging over the fitted $\Delta\chi$, such that the chosen region was between 5 mm starting from the bottom of the cylinder up to 55 mm along the length of the cylinder as highlighted in Fig. 4(a) on the right bounded by the green lines and also in Fig. 5(d) where the same selected region is bounded by the black dotted lines. Note that all the slice-averaged $\Delta\chi$ values are reported in Tables 2-4 with the 95 % confidence limits shown after bootstrapping over the $\Delta\chi$ values chosen in the defined 5 cm region.

2.2.3. *Validation measurements*

Measurement for air: Besides the 3D printed materials, the susceptibility of air was measured for validation of the applied post processing and fitting procedure. Air is weakly paramagnetic due to the presence of oxygen with $\chi_{air} = 0.366$ ppm (calculated and converted to volume susceptibility in SI units from the molar susceptibilities of the gasses present in air provided in [22] for atmospheric pressure and room temperature). χ_{air} differs considerably from the susceptibility of water ($\Delta\chi_{ref} \approx 9.4$ ppm). For this measurement, a 3D printed clear resin hollow tube with a wall thickness of 0.3 mm was utilized to realize a cylindrical air cavity with a diameter of 9.4 mm in this case such that the aspect ratio of the cylinder is almost the same as for all other 3D printed solid cylinders. In this case, the same 50 slices starting from 5 mm from the bottom of the cylinder up to 55 mm were chosen as mentioned above. However, since the difference between the susceptibility of air and water is quite large, there may be stronger partial volume effects. Therefore, two different fits were performed for air: **(1)** with just one layer of pixels surrounding the cylinder water interface were excluded from the fit, similar to the case for all other materials as explained above and shown in Fig. 4(a) on the left; and **(2)** one additional layer of pixels was also excluded in order to be certain to avoid adding pixels that may be sensitive to the fitting process.

High resolution measurements: In order to test if the chosen isotropic voxel resolution of 1 mm is sufficient to extract the geometry of the cylinder (i.e. one tenth of the cylinder diameter, as also chosen in [19]), a higher voxel resolution measurement with 0.5 mm isotropic voxel resolution was also performed for 5 materials to check the reproducibility of the fitted $\Delta\chi$. In this case too, the same method for post processing was performed as explained above, but now by choosing 100 slices for the same 50 mm length along the cylinder.

Table 2
Literature value of the magnetic susceptibility of air (χ_{ref}) and its difference relative to that of water $\Delta\chi_{ref}$ (top two rows). The estimated values obtained from measured field maps are reported below.

Literature Value	$\Delta\chi_{ref} = \chi_{ref} - \chi_{water}$ (ppm)	Absolute $\chi_{ref} = \Delta\chi_{ref} + \chi_{water}$ (ppm)
Air at NTP	9.406	0.366 [22]
Validation measurement with air	**$\Delta\chi_{est} = \chi_{est} - \chi_{water}$ (ppm)**	**Absolute $\chi_{est} = \Delta\chi_{est} + \chi_{water}$ (ppm)**
(1): Remove one layer of pixels around the cylinder-water interface	9.215 ± 0.030	0.175
(2): Remove two layers of pixels around the cylinder-water interface	9.333 ± 0.036	0.293

3. Results

The above-mentioned post-processing procedure was applied for all the materials used. In the following section, first the results for the measurement with air are explained under the section ***'Air'***. Following this validation measurement with air, the results of all the 3D printed materials are listed under the section ***'3D printed materials'*** for 1 mm voxel resolution, along with additional results of 5 materials with 0.5 mm voxel resolution.

Air: Table 2 reports the literature reference value of χ_{ref} and $\Delta\chi_{ref}$ with respect to water for air. Besides, the measured values $\boldsymbol{\Delta}\chi_{est}$ for air with two different conditions used for choosing the region of interest for fitting (explained in Section 2.2.3), are reported. These are as follows:

Case (1): Here the ROI chosen for fitting is the same as for all other materials, i.e. one layer of pixels surrounding the cylinder surface-water interface is excluded to avoid partial volume effects (shown in Fig. 4(a)). With removing one layer of pixels, the slice averaged susceptibility was slightly underestimated to be $\Delta\chi_{est} = 9.215$ ppm with $|\Delta\chi_{ref} - \Delta\chi_{est}| \approx 0.2$ ppm (Table 2).
Case (2): Here, two layers of pixels surrounding the cylinder-water interface are excluded. In this case, the estimate of $\Delta\chi_{est} = 9.33$ ppm is much closer to the reference value of $\Delta\chi_{ref} = 9.4$ ppm with $|\Delta\chi_{ref} - \Delta\chi_{est}| \approx 0.07$ ppm. Infact, the effect due to the thin clear resin tube was also accounted for by including the flux density distribution to the analytical model (Eq. (2)) due to the 0.3 mm thick clear resin cylindrical tube using the estimated susceptibility of Clear resin V4 (in Table 3). Adding this effect, however, did not significantly improve the estimates for air; the dominant factor affecting the fitting process in this case too being the inclusion/exclusion of pixels that suffered from partial volume effects. Indeed, this demonstrates that because of the large susceptibility difference between air and water, the partial volume effects are stronger, and thus exclusion of one additional layer of pixels is appropriate in this case, to ensure that the fitting process is not affected by partial volume effects.

3D printed materials: The averaged susceptibility $\Delta\chi$ over the suitable 50 slices for all materials is reported in Table 3 and depicted in Fig. 7((a)-(b)) for 1 mm voxel resolution. Additionally, the exclusion of an additional layer of pixels (i.e. Case (2) reported for air), was also double-checked for all other materials, but the fitted values of $\Delta\chi$ were not as sensitive to the choice of either case ((1) or (2)) as they were for air, possibly due to a smaller change in susceptibility with respect to water. For instance, for the chosen example material Clear resin V4, the difference in the estimated $\Delta\chi$ from case (1) and (2) was only ≈ 0.03 ppm, indicating that exclusion of only one layer of pixels was sufficient for the 3D printing materials. Hence for all materials the ROI was kept as explained in Methods (Section 2) (Fig. 4(a)) and is only reported for Case (1).

For five materials including PC, Clear V4, Dental LT V2, Durable V1 and Tough 1500 V1, additional measurements were available with a higher isotropic voxel resolution of 0.5 mm (reported in Table 4 with the superscript ^{h}). These values are reported after averaging over the same distance of 50 mm along the length of the cylinder (i.e. 5 mm starting

Table 3
Slice averaged $\Delta\chi$ values (2nd column) and absolute χ (3rd column) for Filaments on the top and Resins on the bottom, for 1 mm voxel resolution measurements. The 4th column reports certain comments for specific materials that are discussed in Section 3. Here the 95 % confidence limits are shown after bootstrapping over the 50 $\Delta\chi$ values.

Material	$\Delta\chi = \chi - \chi_{water}$ (ppm)	Absolute $\chi = \Delta\chi + \chi_{water}$ (ppm)	Comments/ special observations
		Filaments	
ABS 50	2.748 ± 0.021	−6.292	50% infill density (large difference from 100% infill density suggests potential contribution by trapped air and/or water
ABS 100	0.390 ± 0.005	−8.650	100 % infill density
CPE	0.474 ± 0.011	−8.566	
CPE+	0.472 ± 0.002	−8.568	
Nylon	0.007 ± 0.014	−9.033	Suscepibility close to water, but relatively large estimation error
PC	0.704 ± 0.009	−8.337	Was the only material that was sanded for smoothing purposes, (any leftover impurities may be the reason for a larger discrepancy from known literature values)
PLA green	0.950 ± 0.005	−8.091	
PLA red	0.746 ± 0.005	−8.294	
PLA tough	0.703 ± 0.004	−8.337	
PP	0.161 ± 0.037	−8.880	Larger estimation error, was more challenging to print
PETG	0.516 ± 0.004	−8.524	
rPET	0.545 ± 0.003	−8.494	
TPE	0.676 ± 0.006	−8.364	
TPU 85A	0.381 ± 0.009	−8.659	
TPU 95A	0.049 ± 0.007	−8.991	Susceptibility close to water
TPU 98A	0.530 ± 0.022	−8.510	
		Resins	
Clear V4	−0.294 ± 0.004	−9.334	
Dental LT V2	−0.336 ± 0.021	−9.376	
Durable V1	−0.160 ± 0.010	−9.200	
Elastic 50A	−0.012 ± 0.008	−9.052	Susceptibility close to water, but challenging to handle while printing
Flexible 80A	−0.047 ± 0.003	−9.087	Same as above
Rigid 10K	−1.075 ± 0.010	−10.115	
Tough 1500 V1	−0.247 ± 0.004	−9.287	

from the bottom of the cylinder up to 55 mm up along the cylinder's axis). Good agreement was found between both 1 mm and 0.5 mm voxel resolution measurements with the difference in the estimated values being $|\Delta\chi - \Delta\chi^{h}| \approx 0.052$ ppm in the worst case for PC and Durable resin, 0.022 ppm for Tough 1500 V1 resin, 0.014 ppm for Clear V4 resin, and 0.002 ppm in the best case for Dental LT V2 resin (shown in Table 4, column 4). Hence, additional high resolution measurements were not performed for all the materials to reduce scan time as well as data size.

All the materials were found to be diamagnetic with susceptibilities very close to that of water. All filaments were slightly less diamagnetic than water with $\Delta\chi > 0$ (Fig. 7(a)). Here, 0 denotes the susceptibility of water. Note the large difference in ABS 50 (with 50 % infill density) and ABS 100 (with 100 % infill density) which may be attributed to the presence of more air and possibly some water in ABS 50, thus resulting in it being the least diamagnetic of all the materials. This indicates the importance of having a database comprising of such details. All the resins were found to be more diamagnetic than water with $\Delta\chi < 0$ (Fig. 7 (b)). Materials with susceptibilities closest to that of water were identified to be Nylon, TPU 95A and PP from the filaments ranging from $\Delta\chi \approx -0.01$ ppm for Nylon to ≈ 0.16 ppm for PP. However, Nylon and PP also had a relatively higher error in estimation, which could be due to a weaker susceptibility contrast as well as a degraded print quality especially for PP. From the resins, the materials with susceptibilities closest to water were identified to be Elastic 50A, Flexible 80A and Durable V1 ranging from $\Delta\chi \approx -0.012$ ppm for Elastic 50A to $\Delta\chi \approx -0.16$ ppm for Durable V1. Out of these, Elastic 50 A had a relatively higher estimation error, as being an elastic material, the printed cylinder did not have a uniform and smooth surface.

4. Discussion

Our results may be utilized to choose materials suitable for different kinds of MR experiments. For instance, for phase contrast imaging with water (e.g. flow imaging), materials with susceptibilities closer to that of water may be more desirable to reduce any phase difference arising due to the magnetic susceptibility itself. For studies with biological phantoms, materials with susceptibilities matching those of different biological tissues may be used to mimic tissue properties. Since magnetic susceptibility of a material is one factor that influences the MR effective spin-spin relaxation time T_2^* of the imaged nuclei, different materials may be selected based on desired signal contrast, pulse sequence parameters, acquisition time. For example, materials that have susceptibilities closely matching the susceptibility of the fluid may be appropriate in the case where the relaxation time of the fluid should not be considerably shortened such as Nylon, Elastic 50A resin, Flexible 80A resin or TPU 95A. On the other hand, in certain cases where a relatively shorter relaxation time may be beneficial for faster scanning, materials with larger susceptibility differences with respect to the fluid may be desirable such as the filaments like PLA or Rigid 10 K and Dental LT V2 resins (Table 5). Though it must be noted that for such cases, other factors such as the surface smoothness of the printed materials, may also affect the MR relaxation times. In general, when considering appropriate materials for an experiment, the physical properties of a material like flexibility, elasticity, rigidity, temperature resistance are some of the major factors influencing the choice of a material, however knowledge of the magnetic susceptibility of the material itself is an important governing factor, especially in the context of MR experiment design.

Comparison with literature: For materials that are common with those used in previous work, we report the absolute value of the difference between our estimated values $\chi_{measured}$ and the ones reported in literature $\chi_{literature}$. For instance, $|\chi_{measured} - \chi_{literature}|$ for PLA red is 0.21 ppm, PLA green is 0.42 ppm, rPET is 0.24 ppm and Nylon is 0.5 ppm [19, 21]. However, in [19] the values for translucent green PLA and PET, Mylar are reported. We also note that our values of PLA are in much better agreement with those in [19] than in [21]. For instance, our value of PLA tough differs from that in [21] by 4.4 ppm. Similarly, our ABS values are quite different from those reported in [21]. However, our value for ABS 50 matches well with the value for high density black ABS in [21], differing only by about 0.6 ppm. In this case too, the manufacturers are different besides a possibility of the print parameters being different, which are not provided in [21]. Fig. 8 is a heatmap of the materials used in this work (names on y axis and values in 1st column) compared with those used in [19] and [21] (columns 2 and 3 respectively). For certain materials that are similar and not the same as used in this work, extra labels are specified with the names of the materials used in the references. White blanks represent that for a certain material, no

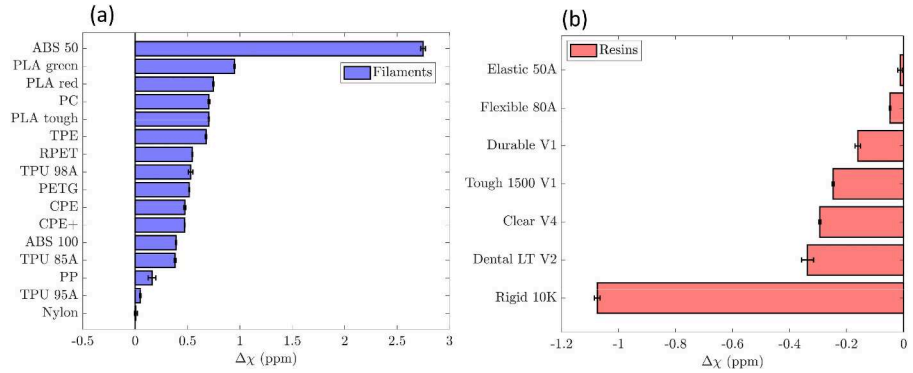

Fig. 7. (a) Slice averaged Δχ with respect to water for all filaments. (b) The same for all the resins. All values of Δχ are plotted in ascending order from bottom to top. The error bars represent the 95 % confidence interval values reported in Table 3.

Table 4
Slice averaged $\Delta\chi^h$ values (2nd column) and absolute χ^h (3rd column) for 5 materials measured with 0.5 mm voxel resolution. The 4th column reports the difference between the estimated Δχ values obtained with 0.5 mm and 1 mm voxel resolution. Here the 95 % confidence limits are shown after bootstrapping over the 100 Δχ values.

Material	$\Delta\chi^h = \chi - \chi_{water}$ (ppm)	Absolute $\chi^h = \Delta\chi^h + \chi_{water}$ (ppm)	$\lvert\Delta\chi - \Delta\chi^h\rvert$ (ppm)
	Filaments		
PC	0.652 ± 0.006 [h]	-8.388 [h]	0.052
	Resins		
Clear V4	-0.280 ± 0.004 [h]	-9.320 [h]	0.014
Dental LT V2	-0.334 ± 0.003 [h]	-9.374 [h]	0.002
Durable V1	-0.212 ± 0.002 [h]	-9.252 [h]	0.052
Tough 1500 V1	-0.225 ± 0.007 [h]	-9.265 [h]	0.022

Table 5
Certain materials along with their potential application/suitability for different MR experiments.

Material	Possible application (with water) based on our results
	Filaments
Nylon TPU 95A	Susceptibility matching: Phase contrast imaging with water, or experiments where T_2^* must not be considerably shortened.
PLA	Larger susceptibility difference: beneficial for faster scanning
	Resins
Elastic 50A Flexible 80A	Susceptibility matching: Phase contrast imaging with water, or experiments where T_2^* must not be considerably shortened.
Rigid 10K Dental LT V2	Larger susceptibility difference: beneficial for faster scanning

data was available in the respective reference.

Our value for Elastic 50A resin compared to the polyurethanes with the same shore hardness reported in [19], for instance their Smooth-On Clear Flex 50 had a $\lvert\chi_{measured} - \chi_{literature}\rvert$ of 0.02 ppm and some of the harder materials such as TPU 85A and TPU 98A compared with Smooth-On Crystal Clear 204 with a shore hardness of 80D differed by about 0.63 and 0.78 ppm respectively. These harder polyurethanes in [19] also are not equivalent in terms of hardness with the ones reported here. Moreover, these were mixtures of various additives and curing agents which may also reflect as a difference to the measurements. Our values for PC and PP had a much larger difference with reported literature of about 1 ppm [17,19,20] and 0.4 ppm [19] respectively. For PP, as mentioned above this may be due to print imperfections, hence resulting in a larger error of the fit. For PC, the large discrepancy and a less diamagnetic value than water was unexpected but the 3D printed cylinder in this case was also smoothed by sanding. Despite cleaning it, some impurities from the sanding process may have affected our estimate. A good agreement with the higher resolution measurements for PC also indicates that this discrepancy may be due to the impurities in the printed cylinder or may also be attributed to it being from a different manufacturer (Stratasys). We did not perform such post processing procedures on any of our other prints to avoid impurities or changes to the print surface quality. The values for the UV cured resin prints differ from some of the resins reported in [19] for instance, by 0.32 ppm for Epotec 201 and Clear resin V4, and by 0.11 for Acryl [21] and Clear Resin V4. However, it must be noted that these may not be equivalent materials due to difference in manufacturing as well as a lack of clear knowledge of the full chemical composition. Another source of difference besides different manufacturers could be that in [19] the filament materials are directly used in the filament form as opposed to printing cylinders. Therefore, knowledge of such parameters like the material manufacturer, printing method, print parameters, post processing of printed objects, may be an important factor to be considered when comparing or reproducing results. Collection of such details in the database will help achieve the goal of having an easily accessible accepted reference of magnetic properties of materials typically used in MR experiments.

5. Summary & conclusions

In this work, we present several contemporarily available and widely used 3D printing materials and measured their magnetic susceptibilities. This was done at a 3T MRI scanner by mapping the field inhomogeneities caused by 3D printed cylinders of each material that were immersed in deionized water serving as a reference medium of known susceptibility. A detailed procedure for acquiring the data, important post processing steps for acquiring the phase map corresponding to phase shifts only due to the magnetic susceptibility, along with the procedure for fitting the obtained data with theory were provided (see Section 2.2). Additionally, our measurement and fitting procedure was verified with a material of known susceptibility (air) and a good agreement was found between our estimates and the literature value (see Section 3). Besides this, for a few materials a higher resolution measurement was also reported and reproduced the estimated values of susceptibility with the lower resolution measurement well, thereby further validating our procedure (Table 4). Based on the estimated magnetic susceptibilities, we also discussed which materials may be suitable in different circumstances. Moreover, the utilization of the exact analytical expressions for a finite sized cylinder improved our estimation while being less computationally expensive and less prone to discretization errors than in a finite difference solution. The susceptibility estimates for some of our materials in common with other references

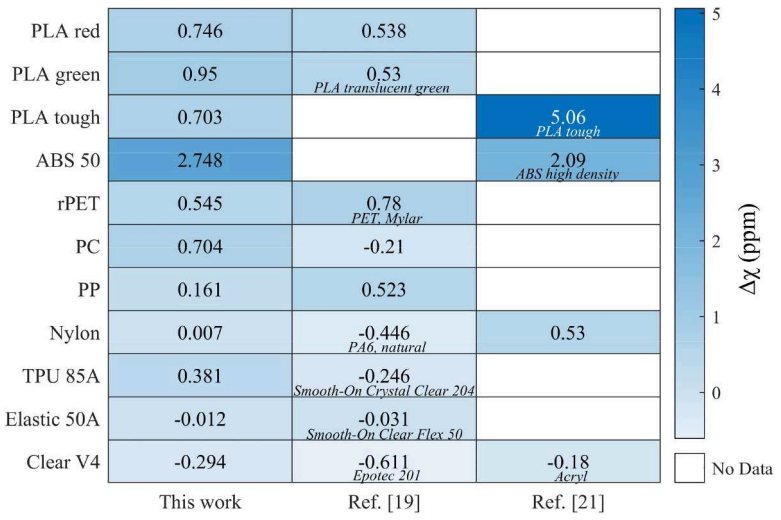

Fig. 8. Heatmap showing a comparison of some of $\Delta\chi$ values of the materials explored in this work with same or similar materials from existing literature.

also showed a good agreement, whereas in some cases they were found to differ significantly from other works (see Section 4). Potential sources for such differences were also discussed. However, this highlights the importance of this work acting as an additional database for magnetic properties of several commonly used 3D printing materials. Not only will this pose useful for selection of materials for an experiment design, it may also drive further studies investigating the magnetic properties of materials, for which a globally accepted reference database does not exist yet, at least to our knowledge. To surmount the lack of such a database, an initiative is taken in this work to not only provide the results reported here but also invite other peers in the scientific community to share their results to build a comprehensive open database for magnetic properties of commonly used materials in MR related experiments. This database may be extended in the future to include properties such as relaxation times, of the MR signal of the fluid under study, when exposed to these 3D printing materials.

Funding

This work was supported by Deutsche Forschungsgemeinschaft (DFG), Sonderforschungsbereich(SFB)/Transregio (TRR) 287 "BULK REACTION" [Project number 422037413].

Declaration of Competing Interest

The authors declare that they have no known competing financial interests or personal relationships that could have appeared to influence the work reported in this paper.

Data availability

The link to our database is provided in the manuscript. This database is open to all and external submissions are welcome for further development and improvement.

Acknowledgements

We express our gratitude to our colleagues who provided integral support and guidance for this work. A special mention to Lucas Knull (Research Campus STIMULATE, Otto-von-Guericke University, Magdeburg), who 3D printed with the filament materials used, Mr. Hannes Schnurre (Dept. of Biomedical Magnetic Resonance, Otto-von-Guericke University, Magdeburg) for his help with printing with an SLA printer and for setting up the material database, Dr. Frank Godenschweger and Ms. Cindy Yvonne Lübeck (Dept. of Biomedical Magnetic Resonance, Otto-von-Guericke University, Magdeburg), Mr. Thomas Gerlach and Mr. Robert Kowal (Research Campus STIMULATE, Otto-von-Guericke University, Magdeburg) for their involvement and efforts in helping with data acquisition and large data export. Part of this work entered Mr. Simon Carl Priese's bachelor thesis.

References

[1] D. Mitsouras, P.C. Liacouras, 3D Printing Technologies, in: F.J. Rybicki, G.T. Grant (Eds.), 3D Print. Med. Pract. Guide Med. Prof, Springer International Publishing, Cham, 2017, pp. 5–22, https://doi.org/10.1007/978-3-319-61924-8_2.
[2] C.Y. Liaw, M. Guvendiren, Current and emerging applications of 3D printing in medicine, Biofabrication 9 (2017), 024102, https://doi.org/10.1088/1758-5090/aa7279.
[3] D. Fan, Y. Li, X. Wang, T. Zhu, Q. Wang, H. Cai, W. Li, Y. Tian, Z. Liu, Progressive 3D printing technology and its application in medical materials, Front. Pharmacol. (2020) 11. https://www.frontiersin.org/articles/10.3389/fphar.2020.00122.
[4] B. Berman, 3-D printing: the new industrial revolution, Bus. Horiz. 55 (2012) 155–162, https://doi.org/10.1016/j.bushor.2011.11.003.
[5] H.Nam Chan, M.J. Andrew Tan, H. Wu, Point-of-care testing: applications of 3D printing, Lab. Chip. 17 (2017) 2713–2739, https://doi.org/10.1039/C7LC00397H.
[6] K.H. Herrmann, C. Gärtner, D. Güllmar, M. Krämer, J.R. Reichenbach, 3D printing of MRI compatible components: why every MRI research group should have a low-budget 3D printer, Med. Eng. Phys 36 (2014) 1373–1380, https://doi.org/10.1016/j.medengphy.2014.06.008.
[7] R. Rai, Y.F. Wang, D. Manton, B. Dong, S. Deshpande, G.P. Liney, Development of multi-purpose 3D printed phantoms for MRI, Phys. Med. Biol. 64 (2019), 075010, https://doi.org/10.1088/1361-6560/ab0b49.
[8] S. Wei, Z. Wang, H. Wang, X. Lyu, L. Deng, W. Yang, Design and implementation of MRI RF coil based on 3D printing, in: Proc. 2015 IEEE MTT- 2015 Int. Microw. Workshop Ser. RF Wirel. Technol. Biomed. Healthc. Appl. IMWS-BIO, 2015, pp. 222–224, https://doi.org/10.1109/IMWS-BIO.2015.7303857.
[9] M. Randazzo, J.M. Pisapia, N. Singh, J.P. Thawani, 3D printing in neurosurgery: a systematic review, Surg. Neurol. Int. 7 (2016) S801–S809, https://doi.org/10.4103/2152-7806.194059.
[10] M.S. Pravdivtseva, E. Peschke, T. Lindner, F. Wodarg, J. Hensler, D. Gabbert, I. Voges, P. Berg, A.J. Barker, O. Jansen, J.B. Hövener, 3D-printed, patient-specific intracranial aneurysm models: from clinical data to flow experiments with endovascular devices, Med. Phys. 48 (2021) 1469–1484, https://doi.org/10.1002/mp.14714.
[11] M.S. Pravdivtseva, F. Gaidzik, P. Berg, C. Hoffman, L.A. Rivera-Rivera, R. Medero, L. Bodart, A. Roldan-Alzate, M.A. Speidel, K.M. Johnson, O. Wieben, O. Jansen, J. B. Hövener, N. Larsen, Pseudo-enhancement in intracranial aneurysms on black-blood MRI: effects of flow rate, spatial resolution, and additional flow suppression, J. Magn. Reson. Imaging. 54 (2021) 888–901, https://doi.org/10.1002/jmri.27587.
[12] L. Chatre, J. Socci, S.J. Adams, P. Denissenko, N. Cherkasov, Design of 3D-printed structures for improved mass transfer and pressure drop in packed-bed reactors, Chem. Eng. J. 420 (2021), 129762, https://doi.org/10.1016/j.cej.2021.129762.
[13] D.A. Clarke, F. Dolamore, C.J. Fee, P. Galvosas, D.J. Holland, Investigation of flow through triply periodic minimal surface-structured porous media using MRI and CFD, Chem. Eng. Sci. 231 (2021), 116264, https://doi.org/10.1016/j.ces.2020.116264.

[14] M. Bruschewski, S. Flint, S. Becker, Magnetic resonance velocimetry measurement of viscous flows through porous media: comparison with simulation and voxel size study, Physics (College Park Md) 3 (2021) 1254–1267, https://doi.org/10.3390/physics3040079.
[15] J.F. Schenck, The role of magnetic susceptibility in magnetic resonance imaging: MRI magnetic compatibility of the first and second kinds, Med. Phys. 23 (1996) 815–850, https://doi.org/10.1118/1.597854.
[16] R.W. Brown, Y.C.N. Cheng, E.M. Haacke, M.R. Thompson, R. Venkatesan, Magnetic Resonance imaging: Physical Principles and Sequence Design, 2nd edition, John Wiley & Sons, Inc, Hoboken, New Jersey, 2014.
[17] F.D. Doty, G. Entzminger, Y.A. Yang, Magnetism in high-resolution NMR probe design. I: general methods, Concepts Magn. Reson. 10 (1998) 133–156, https://doi.org/10.1002/(SICI)1099-0534(1998)10:3<133::AID−CMR1>3.0.CO;2-Y.
[18] L.F. Fuks, F.S.C. Huang, C.M. Carter, W.A. Edelstein, P.B. Roemer, Susceptibility, lineshape, and shimming in high-resolution NMR, J. Magn. Reson. 100 (1992) (1969) 229–242, https://doi.org/10.1016/0022-2364(92)90258-9.
[19] M.C. Wapler, J. Leupold, I. Dragonu, D. von Elverfeld, M. Zaitsev, U. Wallrabe, Magnetic properties of materials for MR engineering, micro-MR and beyond, J. Magn. Reson. 242 (2014) 233–242, https://doi.org/10.1016/j.jmr.2014.02.005.
[20] P.T. Keyser, S.R. Jefferts, Magnetic susceptibility of some materials used for apparatus construction (at 295K), Rev. Sci. Instrum. 60 (1989) 2711–2714, https://doi.org/10.1063/1.1140646.
[21] S. Hwang, S.K. Lee, Efficient experimental design for measuring magnetic susceptibility of arbitrarily shaped materials by MRI, Investig. Magn. Reson. Imaging. 22 (2018) 141, https://doi.org/10.13104/imri.2018.22.3.141.
[22] Chemical Rubber Company, CRC Handbook of Chemistry and physics: a Ready-Reference Book of Chemical and Physical Data, 85, CRC Press, Boca Raton, 2004 ed.
[23] Safety Data Sheet Elastic 50A resin., (n.d.). https://dental-media.formlabs.com/datasheets/2001417-SDS-ENEU-0.pdf.
[24] Safety Data Sheet Clear resin., (n.d.). https://formlabs-media.formlabs.com/datasheets/1801037-SDS-ENEU-0.pdf.
[25] Safety Data Sheet Flexible 80A resin., (n.d.). https://formlabs-media.formlabs.com/datasheets/2001419-SDS-ENEU-0.pdf.
[26] Safety Data Sheet Dental LT V2 resin., (n.d.). https://formlabs-media.formlabs.com/datasheets/2001421-SDS-ENUS-0.pdf.
[27] Safety Data Sheet Durable resin., (n.d.). https://formlabs-media.formlabs.com/datasheets/1801043-SDS-ENEU-0.pdf.
[28] Safety Data Sheet Tough resin., (n.d.). https://formlabs-media.formlabs.com/datasheets/2001295-SDS-ENEU-0.pdf.
[29] Formlabs, Safety Data Sheet Rigid 10K, (n.d.). https://center3dprint.com/files/Rigid_10K_Resin_SDS_(EN).pdf.
[30] J.D. Jackson, Classical Electrodynamics, 3rd ed., Wiley, New York, 1999.
[31] A. Caciagli, R.J. Baars, A.P. Philipse, B.W.M. Kuipers, Exact expression for the magnetic field of a finite cylinder with arbitrary uniform magnetization, J. Magn. Magn. Mater. 456 (2018) 423–432, https://doi.org/10.1016/j.jmmm.2018.02.003.
[32] JAC /QSMbox · GitLab, GitLab. (2021). https://gitlab.com/acostaj/QSMbox (accessed March 6, 2023).
[33] J. Acosta-Cabronero, C. Milovic, H. Mattern, C. Tejos, O. Speck, M.F. Callaghan, A robust multi-scale approach to quantitative susceptibility mapping, Neuroimage 183 (2018) 7–24, https://doi.org/10.1016/j.neuroimage.2018.07.065.
[34] P.B. Roemer, W.A. Edelstein, C.E. Hayes, S.P. Souza, O.M. Mueller, The NMR phased array, Magn. Reson. Med. 16 (1990) 192–225, https://doi.org/10.1002/mrm.1910160203.
[35] S.D. Robinson, K. Bredies, D. Khabipova, B. Dymerska, J.P. Marques, F. Schweser, An illustrated comparison of processing methods for MR phase imaging and QSM: combining array coil signals and phase unwrapping, NMR Biomed 30 (2017) e3601, https://doi.org/10.1002/nbm.3601.
[36] H. Sun, J.O. Cleary, R. Glarin, S.C. Kolbe, R.J. Ordidge, B.A. Moffat, G.B. Pike, Extracting more for less: multi-echo MP2RAGE for simultaneous T1 -weighted imaging, T1 mapping, R2* mapping, SWI, and QSM from a single acquisition, Magn. Reson. Med. 83 (2020) 1178–1191, https://doi.org/10.1002/mrm.27975.
[37] K. Eckstein, B. Dymerska, B. Bachrata, W. Bogner, K. Poljanc, S. Trattnig, S. D. Robinson, Computationally efficient combination of multi-channel phase data from multi-echo acquisitions (ASPIRE), Magn. Reson. Med. 79 (2018) 2996–3006, https://doi.org/10.1002/mrm.26963.
[38] H.S. Abdul-Rahman, M.A. Gdeisat, D.R. Burton, M.J. Lalor, F. Lilley, C.J. Moore, Fast and robust three-dimensional best path phase unwrapping algorithm, Appl. Opt. 46 (2007) 6623–6635, https://doi.org/10.1364/AO.46.006623.
[39] F. Schweser, S.D. Robinson, L. de Rochefort, W. Li, K. Bredies, An illustrated comparison of processing methods for phase MRI and QSM: removal of background field contributions from sources outside the region of interest, NMR Biomed. 30 (2017), https://doi.org/10.1002/nbm.3604.
[40] D. Zhou, T. Liu, P. Spincemaille, Y. Wang, Background field removal by solving the Laplacian boundary value problem, NMR Biomed. 27 (2014) 312–319, https://doi.org/10.1002/nbm.3064.
[41] E. Farrher, J. Lindemeyer, F. Grinberg, A.M. Oros-Peusquens, N.J. Shah, Concerning the matching of magnetic susceptibility differences for the compensation of background gradients in anisotropic diffusion fibre phantoms, PLoS ONE 12 (2017), e0176192, https://doi.org/10.1371/journal.pone.0176192.